

Investigating the deactivation and regeneration mechanism of Fe-based catalysts during CO₂ reduction to chemicals

Juan Manuel Arce-Ramos^a, Wen-Qing Li^a, San Hua Lim^b, Jie Chang^b, Takuya Hashimoto^c, Hiroyuki Kamata^c, Michael B. Sullivan^a, Armando Borgna^b, Luwei Chen^{b,*}, Chee Kok Poh^{b,*}, Jia Zhang^{a,*}

^a Institute of High Performance Computing (IHPC), Agency for Science, Technology and Research (A*STAR), 1 Fusionopolis Way, #16–16 Connexis, Singapore 138632, Republic of Singapore

^b Institute of Sustainability for Chemicals, Energy and Environment (ISCE²), Agency for Science, Technology, and Research (A*STAR), 1 Pesek Road, Jurong Island 627833, Republic of Singapore

^c JII Corporation, 1–1 Toyosu 3-chome, Koto-ku, Tokyo 135-8710, Japan



ARTICLE INFO

Keywords:

Modified Fischer-Tropsch
DFT calculations
Experimental characterization
Fe₅C₂ deactivation
Catalyst regeneration

ABSTRACT

The Modified Fischer-Tropsch process converts CO₂ to chemicals using a dual-function Fe-based catalyst composed typically of magnetite and iron carbides. However, catalyst deactivation limits its industrial application. In this study, we combined Density Functional Theory (DFT) calculations and experiments to provide insights into the underlying catalyst deactivation and regeneration mechanisms. The dynamic state of the catalyst was observed with time on stream, revealing the impact of the evolving reaction mixture along the reactor. Rapid CO₂ and H₂O dissociation on the carbide phase creates persistent ¹⁸O, causing Fe₅C₂ deactivation through oxidation. On the other hand, the direct carburization of Fe₃O₄ proves challenging due to significant energy barriers, underscoring the need for metallic Fe or a highly reduced surface as a precursor to effective catalyst activation. These insights into iron catalyst evolution during CO₂ reduction can guide the development of strategies for achieving efficient catalyst performance.

1. Introduction

Climate change is an urgent environmental issue that humanity faces today, with one of the culprits being the greenhouse gas carbon dioxide (CO₂). The primary source of CO₂ emissions is the burning of fossil fuels, such as coal, oil, and natural gas, for energy production. A potential solution to reduce CO₂ in the atmosphere is to capture it on-site and convert it into valuable chemicals, including fuels. This practice is known as carbon capture and utilization (CCU) and offers the dual benefit of reducing harmful emissions while generating revenue [1].

The Modified Fischer-Tropsch (MFT) process is a promising method for converting CO₂ into chemicals. It involves two sequential reactions [2]: the reverse water-gas shift reaction (RWGS), which produces CO and H₂O from CO₂ and H₂, followed by the Fischer-Tropsch synthesis (FTS), responsible for hydrocarbons and oxygenates production. The MFT process typically operates at temperatures ranging from 200–400 °C and pressures between 1 and 30 bars [2–5]. While the H₂:CO₂ ratios

employed can vary from 1:2 to 4:1, a 3:1 ratio is frequently chosen, aligning with the stoichiometry of the CO₂ to ethylene conversion. The catalyst used in MFT is typically Fe-based, which in its activated form consists of magnetite (Fe₃O₄) and iron carbides (predominantly Fe₅C₂), each playing a specific role during the MFT process. The magnetite phase is thought to facilitate RWGS [6,7], while FTS occurs on the carbide phase.

Indeed, while the Fe-based catalysts show great potential for the MFT process due to their dual functionality, their susceptibility to deactivation hinders wider industrial application. Several mechanisms have been proposed to contribute to catalyst deactivation, including the oxidation of the Fe₅C₂ phase [5,8], catalyst sintering [9,10], carbon deposition [11], and to a lesser extent, the transformation from Fe₅C₂ to Fe₃C [8].

Most existing literature points to the oxidation of the carbide phase, leading to the formation of Fe₃O₄, as the primary deactivation process. Some studies suggest that this oxidation can be triggered by CO₂ and H₂O [12–14], which are the reactant and product respectively in the

* Corresponding authors.

E-mail addresses: chen_luwei@isce2.a-star.edu.sg (L. Chen), poh_chee_kok@isce2.a-star.edu.sg (C.K. Poh), zhangj@ihpc.a-star.edu.sg (J. Zhang).

MFT process. Furthermore, it has been proposed that adjusting the H_2/CO_2 feed ratio can inhibit catalyst oxidation. However, excessive H_2 can promote premature chain termination, leading to an increased production of undesired short hydrocarbons and reducing the efficiency of producing target longer chain products [13]. Thus, a balance must be achieved between H_2 and CO_2 content.

In addition to regulating feed ratios, stabilization of the carbide phase can also be achieved by fine-tuning the chemical potentials of O (e.g., by removing H_2O from the mixture) and C [13]. Should oxidation be the primary cause of deactivation, regeneration of the spent catalyst, or its carburization, may provide a solution. Several studies have demonstrated that oxidized catalysts can be regenerated upon interaction with CO or syngas [14,15], or through a stepwise reduction carburization procedure [14].

Despite these findings, questions regarding the carburization process remain. While some studies report direct conversion of Fe_3O_4 to carbides [16,17], bypassing metallic Fe, others propose a sequence favoring carburization of Fe over FeO and Fe_3O_4 [18], contradicting the former point. It remains ambiguous whether carburization can occur directly from Fe_3O_4 into the carbide phase, necessitating further study for clarification.

The carburization of iron oxides has also been studied using density functional theory (DFT) calculations in some works in the literature. Some studies investigated the carbon-adhering reaction through the Boudouard process ($2\text{CO} \rightarrow *^{\text{C}} + \text{CO}_2$) on an iron oxide surface [19,20]. In both works, it was concluded that the carbon-adhering reaction is unfeasible over iron oxide surfaces. Another DFT work established that the carburization of the Fe_3O_4 (111) surface is thermodynamically favorable when using CO as a carbon source [21]. Han et al. extended this body of research by examining the effect of manganese (Mn) on the carburization of Fe_3O_4 (311) [22]. Their work involved studying the O for C exchange on the Fe_3O_4 surface and determined the carburization to be a favorable process when using CO as the carbon source. This collection of studies reflects the complexity of the carburization process and the potential influence of various factors on its efficiency and outcomes.

While numerous studies have contributed to the understanding of the deactivation process, distinct ambiguities still remain in the mechanism of catalyst deactivation and regeneration. Our work aims to build upon these foundational insights and address the existing gaps in understanding. By combining experimental results with DFT simulations, this study further elucidates these mechanisms. Our investigation provides insights on the oxidation processes of the iron carbide (Fe_5C_2), crucially influencing catalyst deactivation, and the carburization intricacies of magnetite (Fe_3O_4) pertinent to catalyst regeneration. Specifically, we delve into the role of the Fe_5C_2 phase in CO_2 dissociation and the resultant challenges posed by ${}^{\text{O}}$ species accumulation. Importantly, our work unveils the subtle interplay between the Fe_5C_2 and Fe_3O_4 phases in the MFT process, offering insights into optimizing these catalysts' performance.

2. Methods

2.1. Computational methods

We conducted DFT calculations on three different Fe-based surfaces: $\chi\text{-Fe}_5\text{C}_2$ (510) (Fig. 1), $\text{Fe}_{\text{oct}2}$ -terminated Fe_3O_4 (111) (Fig. 2c), and Fe (100) (Fig. 3). Later in this section, we provide a detailed description of the surface models. The VASP software and the projector augmented wave (PAW) method were used for all calculations. We employed the generalized gradient approximation (GGA) and the PBE functional to solve the Kohn-Sham equations, with a cutoff energy of 400 eV for the planewaves. We considered an SCF cycle to be converged when the energy change was below 1×10^{-5} eV, and the atomic forces were deemed to have converged when changes were less than 0.02 eV/Å. To treat partial occupancies, we used the Gaussian smearing method, with a

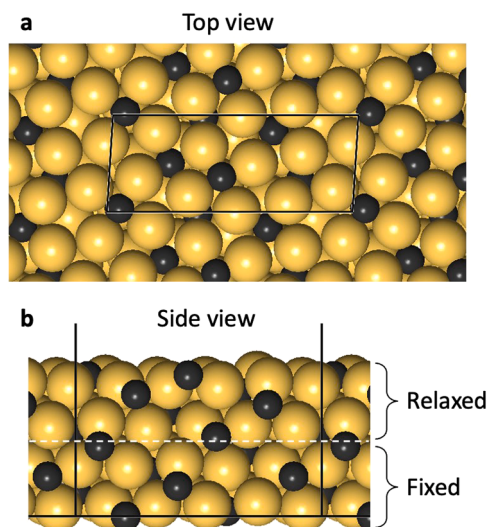


Fig. 1. (1 \times 1) Fe_5C_2 (510) periodic surface model used in this work. Fe and C atoms are shown in yellow and black. The total thickness of the slab was divided in two, where the atoms in the top half were relaxed during optimization, and atoms in the bottom half were fixed at their optimized bulk positions. The limits of the supercell are indicated by black lines.

smearing width of 0.05 eV for Fe_3O_4 . For the metallic systems, Fe and Fe_5C_2 , we used the first-order Methfessel-Paxton scheme with a width of 0.1 eV. In all cases, the total energies were extrapolated to 0 K. Grimme's dispersion correction method (D2) was used to correct van der Waals dispersion forces. Additionally, in accordance with previous studies [23–27], we applied the Hubbard correction method with a U value of 3.7 eV for d-electrons of Fe to accurately describe the electronic states of the Fe_3O_4 material (see Table S1 of the Supplementary Information).

We used reaction energies (ΔE) and activation barriers (E_a) when discussing the energetics of reactions. ΔE is defined as the total energy difference between the products and reactants involved in the corresponding reaction. The activation barriers were calculated by subtracting the total energy of the reactant from the energy of the transition state. The energy of the transition state was obtained via the climbing-image nudged elastic band (CI-NEB) method [28] and the dimer method [29]. A vibrational analysis using the finite differences method was used to validate the identified transition states by a single imaginary frequency mode, characteristic of a first-order saddle point.

2.2. Electronic structure characterization of magnetite (Fe_3O_4)

Magnetite possesses a spinel structure with two types of Fe cations: Fe centers tetrahedrally coordinated with oxygen atoms (Fe_{tet}) with an oxidation state of 3 + and Fe atoms with an octahedral oxygen environment (Fe_{oct}), containing an equal number of $\text{Fe}(2+)$ and $\text{Fe}(3+)$ ions (Fig. 2). The formula of magnetite, $[\text{Fe}(3+)]_{\text{tet}}[\text{Fe}(2+), \text{Fe}(3+)]_{\text{oct}}\text{O}_4$, highlights the electronic and geometric differences between the Fe cations. Magnetite is also a ferrimagnet with a total magnetic moment of 4.0–4.05 μ_{B} per formula unit [29,30], where the magnetic moments of Fe_{tet} and Fe_{oct} atoms are antiferromagnetically coupled. Above the Verwey transition at 120 K, magnetite becomes a semiconductor with a small band gap (between 0.14 and 0.20 eV) [31,32] where small-polaron hopping between $\text{Fe}_{\text{oct}}(2+)$ and $\text{Fe}_{\text{oct}}(3+)$ cations is the primary mechanism for electron mobility [30,31].

We computed the lattice parameter of magnetite to be 8.483 Å, which closely matches the reported experimental values of 8.39 Å [32, 33]. We computed the local magnetic moments of all Fe centers by measuring the spin-charge difference within the atomic sphere using a default value of Wigner-Seitz radius [34], which corresponds to the

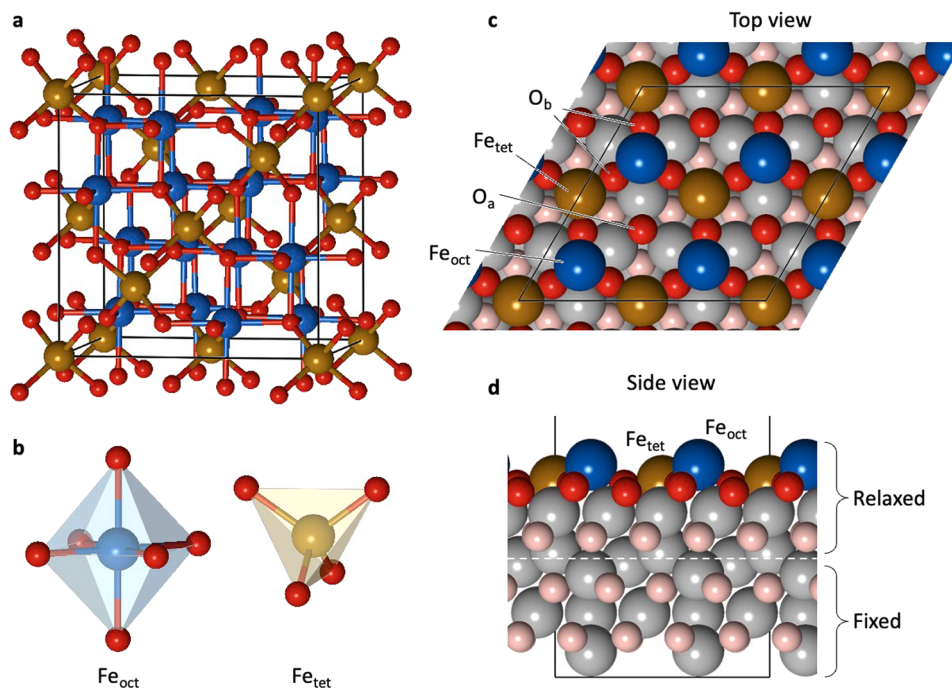


Fig. 2. (a) Depiction of Fe_3O_4 bulk structure showing Fe_{oct} , Fe_{tet} , and O atoms in blue, brown, and red, respectively. The limits of the unit cell are shown as black lines. (b) The local environment of the Fe_{oct} and Fe_{tet} centers. (c) Top and (d) side [010] views of the $\text{Fe}_{\text{oct}2}$ -terminated Fe_3O_4 (111) surface model used in this work. In the $\text{Fe}_{\text{oct}2}$ -terminated surface, surface Fe_{oct} (blue) and Fe_{tet} (brown) atoms have a coordination of three, indicating that surface Fe_{oct} and Fe_{tet} are missing three and one $\text{Fe}-\text{O}$ bonds, respectively, due to surface cleavage. O_a and O_b represent surface oxygen atoms with coordination of three and four, respectively. (Inaccessible) Subsurface Fe and O atoms are shown in gray and pink.

VASP parameter $\text{RWIGS} = -1$. Two distinct Fe_{oct} centers were identified with local magnetic moments of $3.67 \mu_B$ and $4.13 \mu_B$, while all Fe_{tet} centers reported a local magnetic moment of $-4.04 \mu_B$ (Fig. S1 of the Supplementary Information). The computed magnetic moments of Fe_{oct} and Fe_{tet} centers are consistent with those of Fe in FeO ($3.6 \mu_B$) and Fe_2O_3 ($\sim 4.1 \mu_B$). This indicates that Fe_{oct} centers are in either a $2 +$ or $3 +$ oxidation state while an oxidation state of $3 +$ is prevalent for all Fe_{tet} . Additionally, the oxygen atoms do not contribute considerably to the magnetic moment of the material for which we calculated values ranging from $0.01 \mu_B$ to $0.09 \mu_B$ (Fig. S1 of the Supplementary Information). The final total magnetic moment of $4.0 \mu_B$ per formula unit of Fe_3O_4 is in agreement with experimental results [35,36]. The calculated density of states supports the semiconductor nature of magnetite, with the small band gap arising from the occupied d-band states of $\text{Fe}_{\text{oct}}(2 +)$ and unoccupied d-band states of $\text{Fe}_{\text{oct}}(3 +)$ centers (Fig. S2 of the Supplementary Information). Our results, obtained using the PBE+U ($U=3.7$ eV) correction scheme, are consistent with the charge disproportionation between Fe_{oct} atoms and the semiconducting nature of magnetite. In contrast, using a standard Generalized Gradient Approximation (GGA) functional results in a metallic electronic structure and equivalent Fe_{oct} sites, each with an oxidation state of $2.5 +$ (Fig. S3 of the Supplementary Information). The limitations of the standard GGA in accurately representing the strong correlation of Fe 3d-electrons in magnetite are highlighted [37]. This underscores the importance of employing the U correction scheme, specifically designed for handling d-electrons in magnetite.

In addition, in our energy calculations for the Fe_3O_4 surface models, we aimed to highlight the energy variations between reaction steps while maintaining the consistency of the local magnetic moment for the majority of Fe centers. This was achieved by preserving the local environment of Fe centers in consecutive intermediates linked by an elementary reaction step, with the intention of minimizing changes in their magnetic moments. Nevertheless, there were instances where the magnetic moments of certain Fe centers did change, particularly when these centers were directly participating in the reaction. These specific

instances, where direct involvement of Fe centers in bond formation leads to changes in their magnetic moments, are further discussed in Section S1 of the Supplementary Information.

2.3. Surface models

2.3.1. $\chi\text{-Fe}_5\text{C}_2$ (510)

We used the $\chi\text{-Fe}_5\text{C}_2$ (510) surface as built in our previous publication [38]. We showed that the optimized lattice parameters ($a = 11.583 \text{ \AA}$, $b = 4.503 \text{ \AA}$, and $c = 4.987 \text{ \AA}$) agreed with experimental values with a lattice mismatch of -1.7% [38]. The magnetic moment of Fe centers in bulk was $1.73 \mu_B$ on average, consistent with the reported experimental value of $1.72\text{--}1.75 \mu_B$ [39]. We selected the (510) facet of $\chi\text{-Fe}_5\text{C}_2$ as it is often detected in experiments [40]. This surface has been identified as the possible active site during the Fischer-Tropsch synthesis. A periodic (1×1) slab model was used (Fig. 1) to study the stability of relevant intermediates and energy barrier of reactions, with a vacuum region of at least 15 \AA added in the z direction to model the solid-gas interface. The surface slab model comprises four atomic layers, with the 'top' two atomic layers allowed to relax during geometry optimization while the 'bottom' two were kept fixed at the optimized bulk structure. From now on, we refer to this surface model simply as "Fe₅C₂ surface".

2.3.2. Fe_3O_4 (111)

To represent the Fe_3O_4 catalyst, we chose the catalytically relevant (111) surface [23]. The (111) orientation is also the naturally growing orientation of Fe_3O_4 [41]. Magnetite bulk can be cleaved at different positions, leading to six different (111) surfaces (Fig. S4 of the Supplementary Information), with the $\text{Fe}_{\text{oct}2}$ and $\text{Fe}_{\text{tet}1}$ terminations regarded as the most stable ones. While the $\text{Fe}_{\text{oct}2}$ termination is stable at low oxygen chemical potentials, the $\text{Fe}_{\text{tet}1}$ termination is favored under oxidized conditions [42,43]. Additionally, the $\text{Fe}_{\text{oct}2}$ -terminated surface exhibits more favorable CO_2 adsorption compared to the $\text{Fe}_{\text{tet}1}$ termination [44,45]. Thus, we selected the $\text{Fe}_{\text{oct}2}$ termination in our study

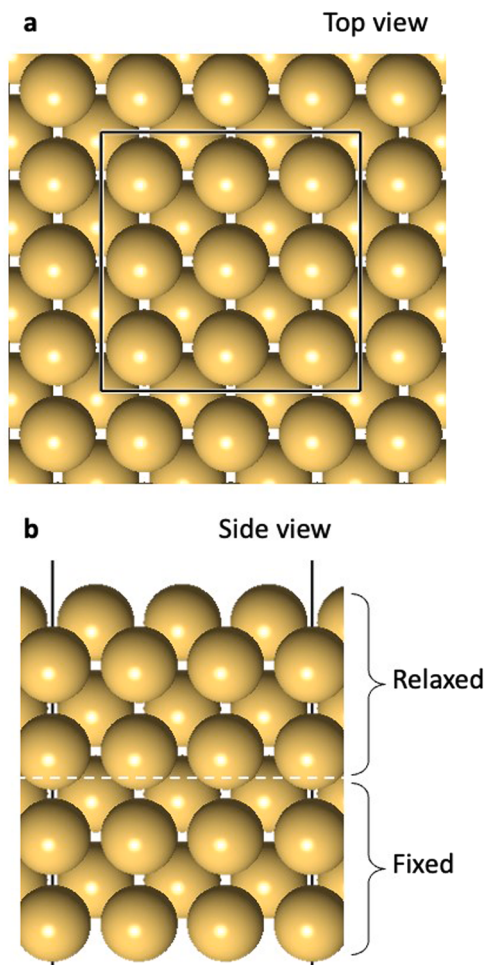


Fig. 3. (3×3) Fe (100) periodic surface model utilized in this study. The black lines indicate the boundaries of the supercell.

(Fig. 2), which exposes both types of Fe centers bound to the surface through three Fe—O bonds. In this manuscript, we refer to the $\text{Fe}_{\text{oct}2-}$ -terminated Fe_3O_4 (111) simply as Fe_3O_4 surface. A (2×2) periodic slab was used to simulate this surface, consisting of four Fe_{oct} and four Fe_{tet} exposed cations. These surface cations exhibit a local magnetic moment of $3.57 \mu_B$ and $-3.58 \mu_B$, respectively, indicating a reduced state (2+). The top 6 atomic layers were relaxed during atomic optimization steps, while the bottom six layers were fixed. A vacuum layer of 15 \AA was added in the z direction.

2.3.3. Fe (100)

In this study, our computational investigations centered on the Fe (100) surface. While both the (110) and (100) orientations of iron are associated with the lowest surface energies, there are significant variations in reactivity between these two. Notably, previous research has indicated that the CO dissociation barriers on the Fe (110) surface are higher than those on the Fe (100) surface [46], making the latter a more promising candidate for our investigations. We used a 3×3 supercell comprising eight atomic layers (Fig. 3). The bottom four atomic layers were kept fixed to represent the bulk-like behavior of the material while the top four atomic layers were allowed to relax. The gas-solid interface was created by adding 15 \AA of vacuum in the z direction between repetitive images of the slab.

2.4. Experimental methods

The Fe-based catalyst was synthesized by the co-precipitation

method and subsequently calcined in air at 450°C for 4 h. The fresh catalyst was loaded in a fixed-bed reactor for the modified Fischer-Tropsch reaction. Prior to the reaction, the reduction of Fe_2O_3 (fresh state of the catalyst) was carried out in pure H_2 at 400°C , at a space velocity of 2000 ml/(g.h) , followed by activation with syngas ($\text{CO:H}_2 = 1:2$) at 300°C , 10 barG and 2000 ml/(g.h) . H_2 and CO_2 were introduced during the MFT reaction at a ratio of 3:1, consistent with stoichiometric requirements for the production of olefins and in line with established protocols in the literature [47]. The reaction was carried out at 300°C , 15 barG, $\text{H}_2/\text{CO}_2 = 3$, and 2000 ml/(g.h) for 920 h, after which the spent catalyst at various locations—top, middle, and bottom—of the catalyst bed was characterized using XRD diffraction.

The XRD characterization was carried out using a Bruker D8 Advance diffractometer with a Cu anode ($\text{Cu K}\alpha$ wavelength = 0.154 nm), operated at 40 kV and 40 mA . XRD spectra were produced in the range of $2\theta = 5$ to 90° at a step width of 0.008° .

3. Results and discussions

3.1. Deactivation of the catalyst

3.1.1. Experimental characterization of spent catalyst

We characterized the catalyst at the various stages of the pretreatment processes via powder X-ray diffraction (XRD) as shown in Fig. 4. The XRD pattern of the fresh catalyst resembles the structure of hematite (Fe_2O_3). The catalyst was first reduced in H_2 gas, and the reduction of Fe_2O_3 produced mainly metallic Fe (Fig. 4, second spectrum from the top). After the catalyst was reduced and activated, the catalyst primarily comprised Fe_5C_2 and Fe_2C carbide phases with minor portions of Fe_3O_4 (third spectrum from the top).

The weight percentage of different iron phases for the activated iron

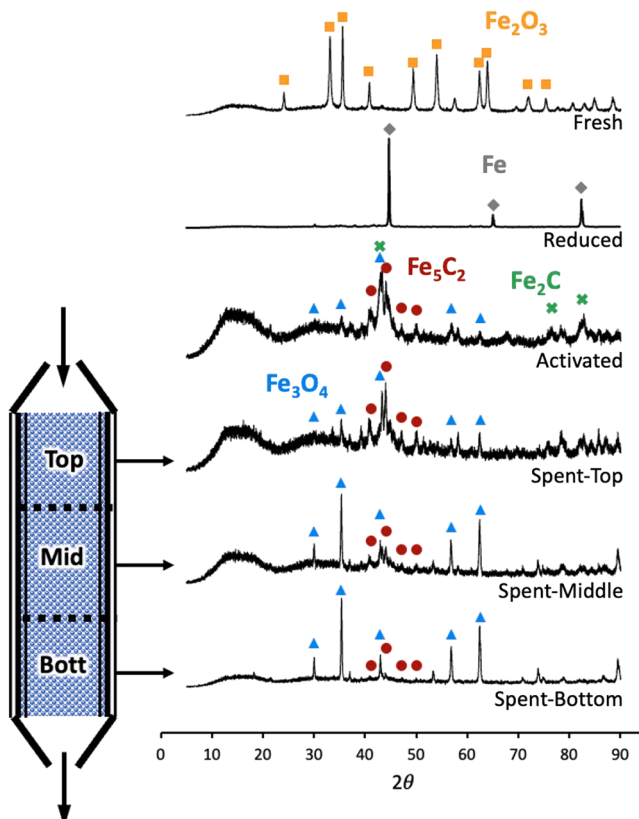


Fig. 4. XRD patterns of spent catalyst samples taken at different stages of the catalyst's bed (top, middle, and bottom). The XRD patterns of the fresh (Fe_2O_3), reduced, and activated catalyst are also presented.

catalyst and spent catalyst at different positions of the reactor is shown in **Table 1**. The activated catalyst has only 2.9 wt% of Fe_3O_4 , and the dominant carbide phase is Fe_2C , which is a carbon-rich phase formed under high carbon chemical potential (μ_{C}) conditions [48]. After the MFT reaction, the spent catalyst showed a clear shift in phase composition. The Fe_2C phase disappeared in the spent catalyst, primarily due to the higher H_2 concentration in the reaction stream ($\text{H}_2/\text{CO}_2 = 3$) and thus reducing the carbon chemical potential and producing Fe_5C_2 with a slightly higher iron-to-carbon ratio. As shown in **Table 1**, the spent catalyst at the top of the reactor, which is close to the entrance of the reactant gases saw an increase in the Fe_3O_4 phase, by close to double after being tested for 920 h, suggesting a preference for oxide formation over carbide during the MFT process. The dominance of Fe_5C_2 near the reactor entrance (top stage) indicates a lesser extent of these oxidizing effects, with its presence diminishing downstream. Near the reactor exit (bottom stage), the catalyst predominantly consisted of Fe_3O_4 , with minute amounts of Fe_5C_2 , as per our XRD characterization. We see an increase of Fe_3O_4 from 5.1 wt% to 57.4 wt% further from the inlet of the reactor. The fraction of iron carbide has been reported to decrease along the catalyst bed upon processing CO_2 [49]. This suggests that the changing environmental conditions, especially the evolving composition of reactants and products, have a significant impact on the predominant equilibrium phase of the catalyst. With increasing distance from the reactor inlet, an elevated concentration of CO , H_2O , and hydrocarbons was anticipated. Among these, water stands out due to its pronounced oxidizing capacity. Specifically, water can oxidize active Fe_5C_2 sites, potentially leading to catalyst deactivation. In fact, water has been reported to have a detrimental effect during CO_2 hydrogenation on Fe-based catalysts [13,50].

To achieve higher stability for the catalytic conversion of CO_2 to hydrocarbons, it is important to investigate the mechanism for this deactivation and propose strategies for the regeneration of the catalyst. In subsequent sections, we will delve into our DFT calculations to explore the formation of surface oxygen species and their removal, which is implicated in the catalyst's deactivation. We will also examine reactions related to regeneration.

3.1.2. Formation of surface oxygen and its elimination on Fe_5C_2

In this section, we explore the energetics of the RWGS occurring on the Fe_5C_2 surface. The RWGS entails activating and dissociating CO_2 to produce $^*\text{CO}$ and $^*\text{O}$, followed by the hydrogenation of $^*\text{O}$ to yield water. The relevance of these reactions arises from the fact that both CO_2 and H_2O dissociation (the reverse of $^*\text{O}$ hydrogenation to water) create $^*\text{O}$ surface species. Thus, the energy dynamics of the RWGS reaction cycle can shed light on a surface's capacity to generate and eliminate surface $^*\text{O}$ species. When referring to specific intermediates, we have assumed that those not participating in the elementary step (deemed spectator) are distanced from the active site, denoted by the “ ∞ ” superscript in **Fig. 5**. In addition, considering the reaction temperature, the Gibbs free energy at 300 °C for the intermediates discussed herein were calculated, **Table S2** of the Supplementary Information. We found that the thermodynamic corrections to elementary surface reactions at 300 °C are in the range of -0.18 eV to 0.07 eV, which will not change our understanding of the reaction mechanism.

As shown in **Fig. 5**, we initially considered the stepwise adsorption of CO_2 and H_2 molecules on the Fe_5C_2 surface. This follows the exothermic

adsorption processes of CO_2 ($\Delta E = -0.98$ eV) and dissociative adsorption of H_2 ($\Delta E = -1.77$ eV), leading to configuration 2 ($^*\text{CO}_2 + 2^*\text{H}^\infty$) in **Fig. 5**. We assumed that H_2 spontaneously forms $^*\text{H}$ surface species. Subsequently, the dissociation of $^*\text{CO}_2$ requires overcoming a barrier of 0.40 eV and has $\Delta E = -1.03$ eV, 3 ($^*\text{CO} + ^*\text{O}$), indicating a highly favorable process. These results are consistent with a previous study of CO_2 on the Fe_5C_2 (510) surface [27]. The co-adsorption of $^*\text{CO}$ and $^*\text{O}$ is repulsive, as evidenced by the $\Delta E = -0.55$ eV upon separating the surface species, 4 ($^*\text{O} + ^*\text{CO}^\infty + 2^*\text{H}^\infty$), i.e., becoming non-interactive. One of the distant $^*\text{H}^\infty$ species approaches the $^*\text{O}$ intermediate, 5 ($^*\text{O} + ^*\text{H}$), with $\Delta E = 0.45$ eV compared to the non-interactive system, followed by forming $^*\text{OH}$ after overcoming a barrier of 1.11 eV, 6. This process is endothermic, $\Delta E = 0.25$ eV. Subsequently, a second surface $^*\text{H}$ species moves closer to $^*\text{OH}$, 7 ($^*\text{OH} + ^*\text{H}$), with $\Delta E = 0.17$ eV due to adsorbate-adsorbate repulsion. The formation of $^*\text{H}_2\text{O}$ is endothermic, $\Delta E = 0.90$ eV, and has a barrier of 1.46 eV, 8. Finally, the desorption of $^*\text{H}_2\text{O}$ (9) has $\Delta E = 0.92$ eV. It is worth noting that, with the inclusion of thermodynamic correction terms at 300 °C, the process is endergonic with $\Delta G = 0.60$ eV (**Table S2** of the Supplementary Information). In addition, the further CO dissociation (energy barrier of 1.51 eV, as we calculated) during the Fischer-Tropsch reaction will produce more O^* on the Fe_5C_2 surface, leading to the catalyst deactivation.

Notably, the RWGS and FTS processes generate water as a product, potentially accumulating in downstream sections of the reactor. Typically, the partial pressure of water is about 6–12% during the MFT process [13]. The formation of H_2O from $^*\text{O}$ species (generated by CO_2 dissociation) is a more energy-intensive process, whereas the reverse dehydrogenation is more favorable (see **Fig. 5**), highlighting its significant role in iron carbide oxidation. As the production and accumulation of water in the reaction mixture progresses, it may be re-adsorbed and dissociated on the catalyst's surface, particularly on Fe_5C_2 , contributing to catalyst oxidation and subsequent deactivation. Our experimental results align with this notion, showing that the proportion of Fe_3O_4 in the spent catalysts is higher towards the reactor's exit than near the entrance, **Fig. 4**.

Our study reaffirms the swift CO_2 dissociation on Fe_5C_2 (**Fig. 5**), prompting questions about the traditionally acknowledged role of Fe_3O_4 in the RWGS. While most research advocates higher RWGS efficiency over iron oxides [3], some evidence shows CO formation from CO_2 on iron carbides [51,52] or other transition metal carbides [53,54]. Our calculations reveal a disparity in the energy requirements for CO_2 dissociation on Fe_3O_4 and Fe_5C_2 ; the former is endothermic and needs to surpass a marginally larger activation barrier of 0.58 eV (**Fig. S6** of the Supplementary Information) compared to the highly exothermic process and a barrier of 0.32 eV on Fe_5C_2 . However, the exothermic hydrogenation of $^*\text{O}$ to $^*\text{H}_2\text{O}$ over Fe_3O_4 , with barriers of 0.41 eV and 0.89 eV, is more favorable than on Fe_5C_2 (endothermic and with barriers of 1.03 eV and 1.19 eV, **Fig. 5**). The removal of O^* species is facilitated on Fe_3O_4 , which promotes the forward RWGS reaction more efficiently than Fe_5C_2 . Thus, the emergence of Fe_3O_4 provides alternative sites for the RWGS reaction without excessive oxidation of the catalyst. Consequently, a moderate oxidation of the carbide phase might not be detrimental to the MFT process. However, if Fe_3O_4 concentrations exceed a certain threshold, the FTS process could become a bottleneck, diminishing the catalyst's efficiency.

In light of these challenges, strategies such as the removal of water and the application of catalyst promoters have been researched extensively [13,55,56]. While common promoters such as alkali metals (Na, K), can improve olefin production, they also strengthen the adsorption of H_2O , potentially promoting the oxidation of the carbide phase. Transition metals like Cr, Mn, Zn, and Co are known to enhance both catalyst stability and olefin production [57,58]. Moreover, a combined promotion using Zn and Na has been shown to mitigate the oxidation of the Fe_5C_2 phase by H_2O and CO_2 [59].

Table 1

The weight percent of different phases of iron from semi-quantitation analysis using DIFFRAC.EVA software from Bruker Corp.

	Fe ₂ C (wt%)	Fe ₅ C ₂ (wt%)	Fe ₃ O ₄ (wt%)
Activated	70.6	26.5	2.9
Spent-top	0	94.9	5.1
Spent-middle	0	76.3	23.7
Spent-bottom	0	42.6	57.4

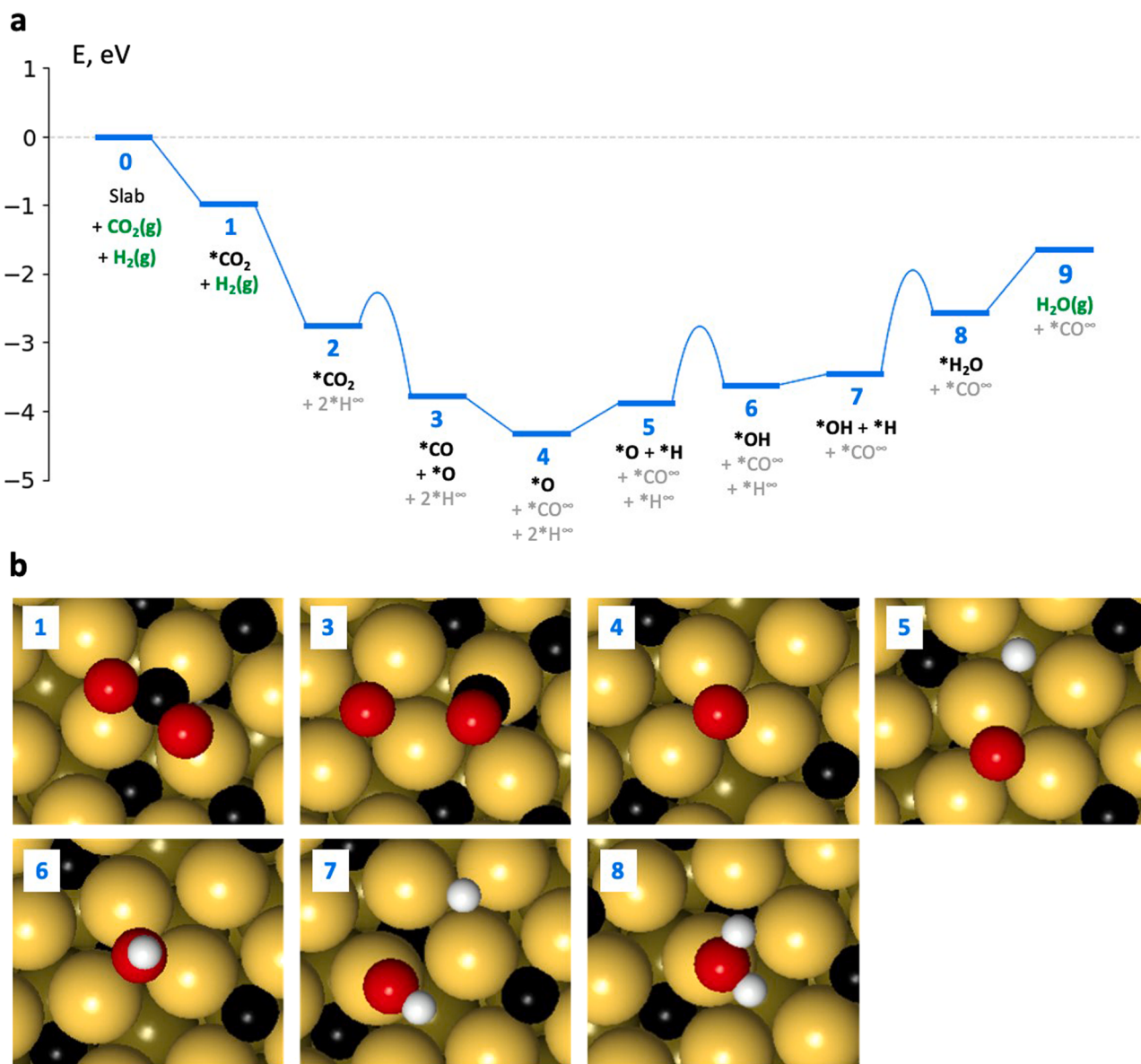


Fig. 5. (a) Potential energy diagram for the RWGS reaction on Fe_5C_2 (510). The curved lines in the diagram represent transition states that connect two intermediate states, with the curve's maximum indicating the transition state energy. (b) Configurations of intermediates in the reaction over Fe_5C_2 . Fe, C, O, and H atoms are color-coded amber, black, red, and white, respectively.

3.2. Carburization (regeneration) of the Fe-based catalyst

Both our simulation results and recent experimental evidence suggests that the oxidation of the Fe_5C_2 phase is the major mechanism for catalyst deactivation [14], emphasizing the significance of understanding the dynamic state of Fe-based catalysts during the MFT process. Though previous research hints at a reversible $\text{Fe}_5\text{C}_2 \leftrightarrow \text{Fe}_3\text{O}_4$ transformation, potentially offering a pathway for catalyst regeneration via adjustment of reaction conditions [13], comprehensive knowledge regarding this process remains scarce despite certain studies proposing the possibility of the Fe-based catalyst's regeneration under syngas or CO atmospheres [14,15]. As shown in Fig. 4, the spent catalyst composition, primarily consisting of magnetite and iron carbides, suggests a direct conversion of iron carbides to Fe_3O_4 . CO-TPD experiments performed on Fe catalysts at various reduction stages (a mix of Fe_3O_4 , FeO , and Fe^0) ascertain that all reduced forms can undergo carburization, with the sequence favoring $\text{Fe}^0 > \text{FeO} > \text{Fe}_3\text{O}_4$ [18]. Nevertheless, the working mechanism of the regeneration of the

Fe-based catalysts is still ambiguous.

Starting from Fe_3O_4 , the whole reaction can be expressed as $\text{O}_{\text{latt}} + 2 \text{H}_2(\text{g}) + \text{CO}(\text{g}) \rightarrow \text{C}_{\text{latt}} + 2 \text{H}_2\text{O}(\text{g})$, which can be broken down into three sequential steps: 1) removal of lattice oxygen (O_{latt}) from Fe_3O_4 in the form of H_2O gas via hydrogenation, $\text{O}_{\text{latt}} + \text{H}_2(\text{g}) \rightarrow \text{H}_2\text{O}(\text{g})$; 2) dissociation of CO to form lattice C_{latt} and surface $^*\text{O}$ ($\text{CO}(\text{g}) \rightarrow \text{C}_{\text{latt}} + ^*\text{O}$); and 3) hydrogenation of $^*\text{O}$ generated from $^*\text{CO}$ to form the second H_2O . Following this reaction framework, we performed detailed investigations into each of these steps. Assuming syngas is used to regenerate the Fe-based catalyst, to elucidate the carburization mechanism of Fe_3O_4 to Fe_5C_2 , we investigated the O vacancy creation via H_2 or CO dissociation over pristine Fe_3O_4 (hereafter referred to simply as Fe_3O_4), Fe_3O_4 with an O vacancy ($\text{O}_{\text{vac}}\text{-Fe}_3\text{O}_4$) and metallic Fe, respectively, to assess the feasibility of the carburization.

3.2.1. Formation of oxygen vacancies on the Fe_3O_4 surface

During our experimental procedures, the fresh catalyst is predominantly reduced to metallic Fe prior to carburization, consequently

resulting in iron carbides and minor proportions of oxide phases (Fig. 4). The degree of reduction in the oxide catalysts inversely correlates with the difficulty of carburization, with a higher reduction degree facilitating easier carburization [18]. To investigate how the reduction influence the carburization process, we developed a theoretical model of the Fe_3O_4 surface with an oxygen vacancy. This allows us to simulate and examine the catalytic surface's behavior under conditions where the oxide is partially reduced. There are two types of surface oxygen atoms, namely O_a and O_b , where O_a can be removed more readily from the surface than O_b by 1.31 eV. Thus, in our simulations, the oxygen vacancy was created by removing one out of four O_a atoms, as depicted in Fig. 2. With this groundwork laid out, we will now delve into the formation mechanism of the oxygen vacancy on the Fe_3O_4 surface. For clarity, Fig. 6 outlines three mechanisms for oxygen vacancy formation on Fe_3O_4 : (1) single H_2 dissociation; (2) double H_2 dissociation; and (3) CO oxidation.

To begin, we explored the single H_2 dissociation pathway. The chemisorption of H_2 on the oxide phase may occur through a homolytic or heterolytic dissociation of the $\text{H}-\text{H}$ bond. In metal oxides, the homolytic dissociation of H_2 produces two protons (H^+) generally attached to lattice O anions [60]. During the heterolytic dissociation of H_2 , one proton and one hydride are formed, the latter attached to a lattice cation. Initially, the H_2 molecule approaches the surface near the under-coordinated oxygen site (11, Fig. 6). The heterolytic dissociation of H_2 is favored over the homolytic one due to its polarization near the surface ionic species, i.e., $\text{Fe}(3+/2+)$ and $\text{O}(2-)$ [60]. The heterolytic dissociation leads to one hydride (H^-) and one proton (H^+) binding to

respectively a Fe and an O site (12). The dissociation is exothermic, with a reaction energy of -0.86 eV, and has an energy barrier of 0.20 eV. The migration of the H^- from a Fe_{oct} site to an oxygen site (as a proton, H^+) involves the transfer of two electrons to the slab (13), effectively reducing the total magnetic moment of the system from $72 \mu_B$ to $70 \mu_B$. This process requires overcoming a sizable energy barrier of 1.85 eV. $^*\text{H}_2\text{O}$ is then produced when the proton from the bridging $^*\text{OH}$ migrates to the $^*\text{OH}$ at the center of the hexagonal $(\text{Fe}_{\text{oct}}\text{Fe}_{\text{tet}})_3\text{O}_6$ unit (14). The desorption of $^*\text{H}_2\text{O}$ (15) leaves an oxygen vacancy on the surface slab, which is referred to as $\text{O}_{\text{vac}}\text{-Fe}_3\text{O}_4$ surface (15).

Due to a large energy barrier for the migration of H^- from a Fe_{oct} site to a neighboring oxygen (12→13), we further explored a double H_2 dissociation pathway for the formation of an oxygen vacancy. From configuration 12, a second H_2 molecule may approach a free surface Fe_{oct} site (16, Fig. 6), dissociating heterolytically, forming a second H^- bound to a Fe_{oct} site and an additional H^+ binding the OH, leading to adsorbed H_2O (17). In this case, the dissociation has a reaction energy of 0.46 eV and requires overcoming a barrier of 0.50 eV. At this point, two Fe-binding H^- remain on the surface besides $^*\text{H}_2\text{O}$. After one of the H^- migrates to a neighboring surface Fe_{tet} site (18, $\Delta E = 0.64$ eV and $E_a = 1.12$ eV), the two H^- are close enough to form H_2 (19, $\Delta E = -0.71$ eV and $E_a = 0.51$ eV). The subsequent desorption of H_2 and H_2O produces $\text{O}_{\text{vac}}\text{-Fe}_3\text{O}_4$ (15).

In addition to having H_2 as a reductant, as reported by other experiments, a pure CO atmosphere can also facilitate the reduction of Fe_3O_4 [61–63,66]. In light of this, we investigated the CO-induced alternative pathway for the creation of oxygen vacancies on the Fe_3O_4

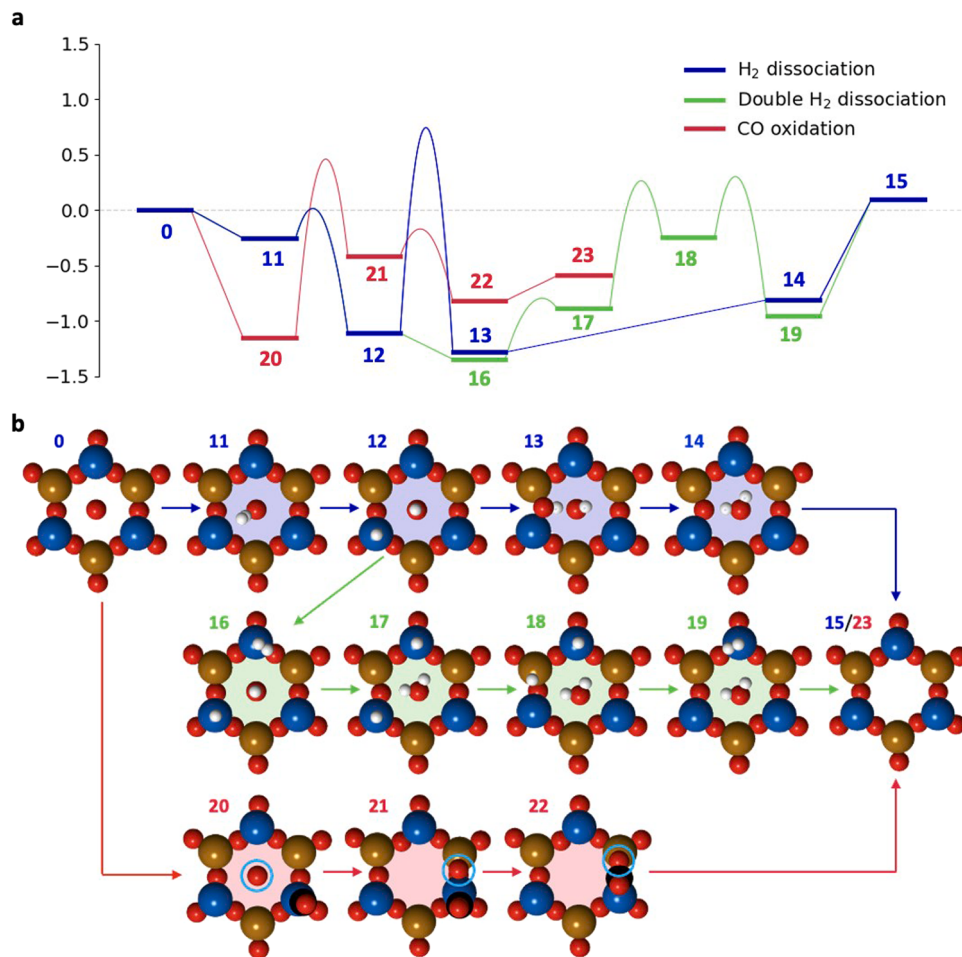


Fig. 6. (a) Potential energy diagram for the formation of an oxygen vacancy on the pristine Fe_3O_4 (111) surface through a single H_2 dissociation (blue), double H_2 dissociation (green), or CO oxidation (red). A smooth line is drawn when there is a transition state linking two intermediate states. (b) Images of the corresponding configurations showing only six Fe centers and their local oxygen environment, focusing on the hexagonal $(\text{Fe}_{\text{oct}}\text{Fe}_{\text{tet}})_3\text{O}_6$ unit.

surface, depicted by the red pathway in Fig. 6 (CO oxidation). After CO is adsorbed on the Fe_3O_4 surface with ΔE of -1.16 eV (20), the neighboring lattice O migrates to a bridge site in between Fe_{oct} and Fe_{tet} surface sites (21, the O at the bridge site is denoted as ${}^*\text{O}_{\text{br}}$). The migration of the lattice O is the most energetically demanding in the CO oxidation mechanism with ΔE of 0.74 eV and E_a of 1.59 eV. ${}^*\text{CO}$ react with ${}^*\text{O}_{\text{br}}$ forming ${}^*\text{CO}_2$ (22, $\Delta E = -0.41$ eV and $E_a = 0.22$ eV). The desorption of ${}^*\text{CO}_2$ (23) has a reaction energy of 0.23 eV. Although most of the elementary steps in the oxidation of CO are thermodynamically and kinetically feasible, the migration of the O atom to the bridge site will hinder this reaction pathway. Therefore, we conclude that the reduction of the Fe_3O_4 surface, at least from its fully oxidized form, proceeds more favorably through the double H_2 dissociation pathway. To understand the influence of the reaction temperature on the energetics, we calculated the reaction and activation free energies for the double H_2 dissociation pathway at 300 °C, Table S3 of the Supplementary Information. The thermodynamic corrections to surface reaction and activation energies are in the range of -0.06 eV to 0.26 eV. Thus, it will not influence the understanding of the reaction mechanism.

3.2.2. Investigating carburization: CO dissociation and lattice C formation

In this section, we further investigate the dissociation of CO on the Fe_3O_4 and $\text{O}_{\text{vac}}\text{-Fe}_3\text{O}_4$, and compare it with that of metallic Fe. As shown in other experiments, a CO atmosphere can trigger the Fe_3O_4 to Fe_5C_2 transformation [14,15]. However, it remains ambiguous if direct oxide-to-carbide conversion is possible. This comparison aims to yield insights into the potential carburization ability of the oxide surface in relation to Fe.

CO prefers to adsorb on the exposed Fe_{oct} sites on both Fe_3O_4 and $\text{O}_{\text{vac}}\text{-Fe}_3\text{O}_4$, with reaction energies of -1.16 eV and -1.24 eV (Figs. 7a and 7b). The subsequent cleavage of the C—O bond leads to Fe_{oct} -bound ${}^*\text{C}$ and an ${}^*\text{O}$ in a bridging position between the two adjacent Fe_{oct} and Fe_{tet} sites. The reaction is highly endothermic, with reaction energies of 3.87 eV and 4.03 eV on the Fe_3O_4 or $\text{O}_{\text{vac}}\text{-Fe}_3\text{O}_4$ surface models, respectively. In the case of $\text{O}_{\text{vac}}\text{-Fe}_3\text{O}_4$, the ${}^*\text{C}$ derived from the ${}^*\text{CO}$ dissociation is most likely to migrate to heal the oxygen vacancy, resulting in ${}^*\text{C}[\text{O}_{\text{vac}}]$, Fig. 7b. It has been found that the co-adsorption of (${}^*\text{C}[\text{O}_{\text{vac}}]$ + ${}^*\text{O}$) is more stable than that of (Fe_{oct} -bound ${}^*\text{C}$ + ${}^*\text{O}$) by 1.36 eV on $\text{O}_{\text{vac}}\text{-Fe}_3\text{O}_4$. However, our calculations indicated that the conversion of ${}^*\text{CO}$ into (${}^*\text{C}[\text{O}_{\text{vac}}]$ + ${}^*\text{O}$) is still a highly endothermic

process, $\Delta E = 2.67$ eV, which makes this process unlikely under typical reaction conditions. Thus, the significant energy demands for CO dissociation on Fe_3O_4 suggest that the carburization is less likely to occur on the oxide surface directly.

To provide more insights into the catalyst regeneration, the energy required to replace lattice oxygen (O_a or O_b , Fig. 2c) with surface carbon (${}^*\text{C}$) over the Fe_3O_4 catalyst was further evaluated from the thermodynamic point of view. Replacing O_a or O_b incurs a reaction energy of 1.71 eV and 1.82 eV, respectively, which is calculated according to the chemical equation $\text{O}_{a/b} + 2 \text{H}_2(\text{g}) + \text{CO}(\text{g}) \rightarrow {}^*\text{C}[\text{O}_{\text{vac}-a/b}] + 2 \text{H}_2\text{O}(\text{g})$. Here, $\text{O}_{a/b}$ represents the energy of the perfect Fe_3O_4 surface slab with O_a and O_b , and ${}^*\text{C}[\text{O}_{\text{vac}-a/b}]$ represents the energy of the surface slab where O_a or O_b has been replaced by C. The thermodynamically unfavorable carbon-oxygen exchange process hints at the poor carburization ability of the Fe_3O_4 catalyst, further suggesting that the surface has to be highly reduced before it can be carburized.

As we discussed above, among the elementary reactions involved in the carburization, the dissociation of CO to form ${}^*\text{C}$ and ${}^*\text{O}$ is the most difficult regardless of the presence of an O vacancy (Fig. 7); thus this step is the bottleneck for the direct carburization of the iron oxide catalyst. Our further simulation work indicated that the C—O dissociation reaction is much more favorable on the metallic Fe (100) surface. As shown in Fig. 7c, the adsorption of CO is exothermic with a ΔE of -2.50 eV. The subsequent dissociation of the C—O bond requires overcoming a barrier of only 0.95 eV, and the reaction is an exothermic process with $\Delta E = -1.00$ eV. These results are consistent with others in the literature [64,65]. When comparing CO dissociation over Fe_3O_4 with or without the O vacancy, it strongly implies that the regeneration of the iron-based catalyst is most likely to take place through metallic Fe. In line with these simulations, our XRD experimental results (as shown in Fig. 4) revealed the presence of metallic Fe after H_2 pre-treatment, highlighting its role during the catalyst activation (via carburization). This observation in the experiments complements and corroborates our simulation results regarding the significance of the metallic Fe.

4. Conclusions

In this work, we explored the reaction mechanisms behind deactivation and regeneration of Fe-based catalysts in MFT reactions. Our investigation suggests catalyst deactivation primarily stems from the

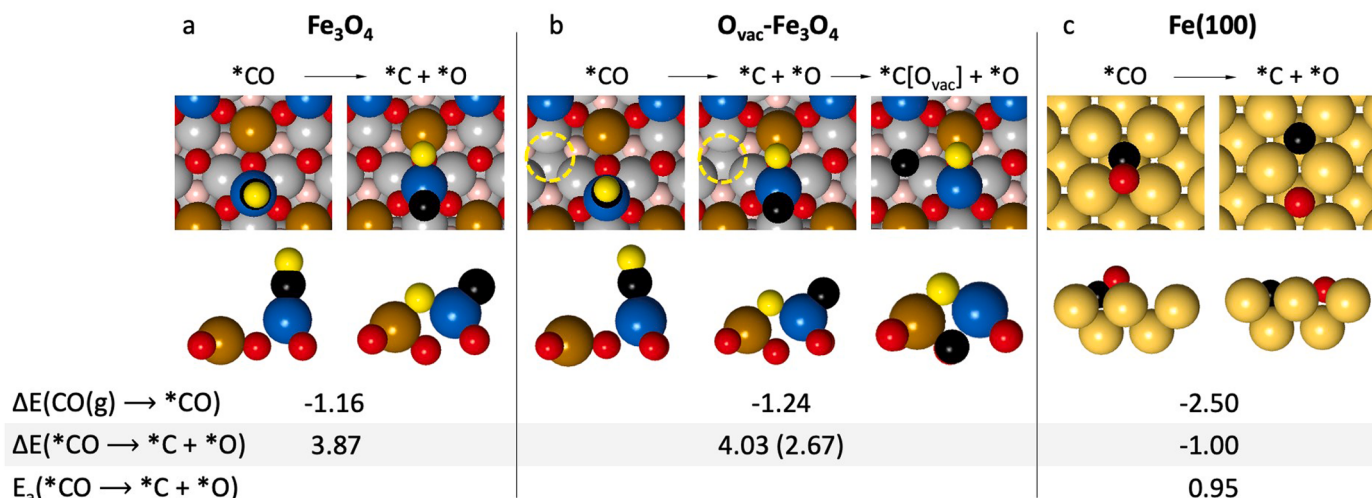


Fig. 7. Adsorbed intermediates involved in the dissociation of ${}^*\text{CO}$ on (a) Fe_3O_4 , (b) $\text{O}_{\text{vac}}\text{-Fe}_3\text{O}_4$, and (c) Fe (100) surfaces. The adsorption energy of CO(g) , $\Delta E(\text{CO(g)} \rightarrow {}^*\text{CO})$, and reaction energy of ${}^*\text{CO}$ dissociation, $\Delta E({}^*\text{CO} \rightarrow {}^*\text{C} + {}^*\text{O})$, are provided. The activation energy for ${}^*\text{CO}$ dissociation, E_a , is also provided for Fe (100). For $\text{O}_{\text{vac}}\text{-Fe}_3\text{O}_4$, two ${}^*\text{CO}$ dissociation products are depicted. In the first product, ${}^*\text{C}$ binds to the Fe_{oct} center, with its corresponding energy (ΔE) as the first listed number. Alternatively, ${}^*\text{C}$ occupies the oxygen vacancy, referred to as ${}^*\text{C}[\text{O}_{\text{vac}}]$, with its reaction energy (ΔE) denoted by the number provided in parenthesis. Fe and O atoms from the Fe_3O_4 surface slab follow the same color code of Fig. 2. For ease of distinction, the oxygen atom derived from CO is colored yellow in the first two panels, contrasting with the lattice O. The location of the oxygen vacancy in $\text{O}_{\text{vac}}\text{-Fe}_3\text{O}_4$ is denoted by a yellow circle.

difficulty in removing surface oxygen species formed by CO_2 and H_2O dissociation on the Fe_5C_2 surface. DFT calculations show that while forming these species is energetically favorable due to exothermic reactions, their elimination is impeded by high thermodynamic and kinetic barriers. Our results also suggest a more intricate role for Fe_3O_4 than previously understood. Traditionally seen as effective in the RWGS reaction, our findings reveal that Fe_5C_2 also significantly contributes to CO formation from CO_2 . Fe_3O_4 , although demanding higher energy for CO_2 dissociation, more efficiently facilitates oxygen removal than Fe_5C_2 , making it a potential alternative site for the RWGS reaction.

Furthermore, we investigated the regeneration of spent catalysts, mainly consisting of iron oxide. We focused on the carburization potential of Fe_3O_4 , examining steps like oxygen vacancy formation and CO dissociation. Our results indicate that the energetically demanding CO dissociation hinders Fe_3O_4 direct carburization. These findings, supported by experimental evidence, imply that Fe_3O_4 must undergo reduction before effective carburization. This study not only clarifies the complex factors in catalyst deactivation and regeneration in Fe-based systems but also advances catalyst utilization in MFT processes. By revealing the nuanced functions of Fe_5C_2 and Fe_3O_4 and emphasizing the importance of the reduction phase, our research opens new avenues for optimizing catalyst design and operational conditions.

Acknowledgments

This work was supported by the A*STAR AME IAF-PP (Grant No. A19E9a0103). The authors acknowledge high-performance computational facilities from the National Supercomputing Centre (NSCC) Singapore (<https://www.nscc.sg>) and A*STAR Computational Resource Centre (A*CRC). We would like to express our gratitude to Mr. Shi Chang Teo, and the Advanced Characterization and Instrumentation (ACI) division from ISCE² for their technical support.

CRediT authorship contribution statement

Li Wen-qing: Formal analysis, Investigation, Writing – review & editing. **Arce Ramos Juan Manuel:** Formal analysis, Investigation, Visualization, Writing – original draft. **Zhang Jia:** Conceptualization, Funding acquisition, Supervision, Writing – review & editing. **Poh Chee Kok:** Conceptualization, Investigation, Supervision, Writing – review & editing. **Chen Luwei:** Conceptualization, Supervision, Writing – review & editing. **Borgna Armando:** Funding acquisition, Supervision. **Sullivan Michael B.:** Funding acquisition, Supervision. **Kamata Hiroyuki:** Formal analysis, Investigation. **Hashimoto Takuya:** Formal analysis, Investigation. **Chang Jie:** Formal analysis, Investigation, Writing – review & editing. **Lim San Hua:** Formal analysis, Investigation.

Declaration of Competing Interest

The authors declare that they have no known competing financial interests or personal relationships that could have appeared to influence the work reported in this paper.

Data Availability

Data will be made available on request.

Appendix A. Supporting information

Supplementary data associated with this article can be found in the online version at [doi:10.1016/j.apcatb.2024.123794](https://doi.org/10.1016/j.apcatb.2024.123794).

References

- M. Ronda-Lloret, G. Rothenberg, N.R. Shiju, A critical look at direct catalytic hydrogenation of carbon dioxide to olefins, *ChemSusChem* 12 (2019) 3896–3914, <https://doi.org/10.1002/cssc.201900915>.
- M. Tavares, G. Westphalen, J.M. Araujo Ribeiro de Almeida, P.N. Romano, E. F. Sousa-Aguiar, Modified fischer-tropsch synthesis: a review of highly selective catalysts for yielding olefins and higher hydrocarbons, *Front. Nanotechnol.* 4 (2022) 1–16, <https://doi.org/10.3389/fnano.2022.978358>.
- B. Pawelec, R. Guill-López, N. Mota, J. Fierro, R. Navarro Yerga, Catalysts for the conversion of CO_2 to low molecular weight olefins—a review, *Materials* 14 (2021) 6952, <https://doi.org/10.3390/ma14226952>.
- Q. Zhang, L. Pastor-Pérez, Q. Wang, T. Ramirez Reina, Conversion of CO_2 to added value products via rWGS using Fe-promoted catalysts: carbide, metallic Fe or a mixture, *J. Energy Chem.* 66 (2022) 635–646, <https://doi.org/10.1016/j.jec.2021.09.015>.
- J. Gorimbo, A. Muleja, X. Liu, D. Hildebrandt, Fischer-Tropsch synthesis: product distribution, operating conditions, iron catalyst deactivation and catalyst speciation, *Int. J. Ind. Chem.* 9 (2018) 317–333, <https://doi.org/10.1007/s40090-018-0161-4>.
- C.-Y. Chou, J.A. Loiland, R.F. Lobo, Reverse water-gas shift iron catalyst derived from magnetite, *Catalysts* 9 (2019) 773, <https://doi.org/10.3390/catal90090773>.
- S.J. Han, S.-M. Hwang, H.-G. Park, C. Zhang, K.-W. Jun, S.K. Kim, Identification of active sites for CO_2 hydrogenation in Fe catalysts by first-principles microkinetic modelling, *J. Mater. Chem. A Mater. 8* (2020) 13014–13023, <https://doi.org/10.1039/DOTA01634A>.
- S. Li, J. Yang, C. Song, Q. Zhu, D. Xiao, D. Ma, Iron carbides: control synthesis and catalytic applications in CO_x hydrogenation and electrochemical HER, *Adv. Mater.* 31 (2019) 1901796, <https://doi.org/10.1002/adma.201901796>.
- S. Gupta, V.K. Jain, D. Jagadeesan, Fine tuning the composition and nanostructure of fe-based core-shell nanocatalyst for efficient CO_2 hydrogenation, *ChemNanoMat* 2 (2016) 989–996, <https://doi.org/10.1002/cnma.201600234>.
- H. Li, W. Li, Z. Zhuang, F. Liu, L. Li, Y. Lv, Z. Men, Z. Liu, Z. Yan, Effect of reaction temperature and H_2/CO ratio on deactivation behavior of precipitated iron Fischer-Tropsch synthesis catalyst, *Catal. Today* 405–406 (2022) 277–284, <https://doi.org/10.1016/j.cattod.2022.04.025>.
- S.-C. Lee, J.-S. Kim, W.C. Shin, M.-J. Choi, S.-J. Choung, Catalyst deactivation during hydrogenation of carbon dioxide: effect of catalyst position in the packed bed reactor, *J. Mol. Catal. A Chem.* 301 (2009) 98–105, <https://doi.org/10.1016/j.molcata.2008.11.016>.
- H. Zhao, J.-X. Liu, C. Yang, S. Yao, H.-Y. Su, Z. Gao, M. Dong, J. Wang, A.I. Rykov, J. Wang, Y. Hou, W.-X. Li, D. Ma, Synthesis of iron-carbide nanoparticles: identification of the active phase and mechanism of Fe-based fischer-tropsch synthesis, *CCS Chem.* 3 (2021) 2712–2724, <https://doi.org/10.31635/ccschem.020.202000555>.
- J. Zhu, P. Wang, X. Zhang, G. Zhang, R. Li, W. Li, T.P. Sengl, W. Liu, J. Wang, Y. Wang, A. Zhang, Q. Fu, C. Song, X. Guo, Dynamic structural evolution of iron catalysts involving competitive oxidation and carburization during CO_2 hydrogenation, *Sci. Adv.* 8 (2022), <https://doi.org/10.1126/sciadv.abm3629>.
- Y. Zhang, C. Cao, C. Zhang, Z. Zhang, X. Liu, Z. Yang, M. Zhu, B. Meng, J. Xu, Y.-F. Han, The study of structure-performance relationship of iron catalyst during a full life cycle for CO_2 hydrogenation, *J. Catal.* 378 (2019) 51–62, <https://doi.org/10.1016/j.jcat.2019.08.001>.
- J. Gorimbo, X. Lu, X. Liu, Y. Yao, D. Hildebrandt, D. Glasser, Low-pressure fischer-tropsch synthesis: in situ oxidative regeneration of iron catalysts, *Ind. Eng. Chem. Res.* 56 (2017) 4267–4274, <https://doi.org/10.1021/acs.iecr.7b00008>.
- Y. Jin, A.K. Datye, Phase transformations in iron fischer-tropsch catalysts during temperature-programmed reduction, *J. Catal.* 196 (2000) 8–17, <https://doi.org/10.1006/jcat.2000.3024>.
- H. Jung, W.J. Thomson, Dynamic X-ray diffraction study of an unreduced iron oxide catalyst in fischer-tropsch synthesis, *J. Catal.* 139 (1993) 375–382, <https://doi.org/10.1006/jcat.1993.1033>.
- M. Ding, Y. Yang, B. Wu, Y. Li, T. Wang, L. Ma, Study on reduction and carburization behaviors of iron phases for iron-based Fischer-Tropsch synthesis catalyst, *Appl. Energy* 160 (2015) 982–989, <https://doi.org/10.1016/j.apenergy.2014.12.042>.
- H. Zhong, L. Wen, C. Zou, S. Zhang, C. Bai, Density functional theory study on the carbon-adhering reaction on $\text{Fe}_3\text{O}_4(111)$ surface, *Metall. Mater. Trans.* 46 (2015) 2288–2295, <https://doi.org/10.1007/s11663-015-0379-x>.
- H. Cheng, D.B. Reiser, S. Dean, On the mechanism and energetics of Boudouard reaction at $\text{FeO}(100)$ surface: $2\text{CO} \rightarrow \text{C} + \text{CO}_2$, *Catal. Today* 50 (1999) 579–588, [https://doi.org/10.1016/S0920-5861\(98\)00492-1](https://doi.org/10.1016/S0920-5861(98)00492-1).
- T. Yang, X. Wen, C. Huo, Y. Li, J. Wang, H. Jiao, Carburization of the $\text{Fe}_3\text{O}_4(111)$ surface, *J. Phys. Chem. C* 112 (2008) 6372–6379, <https://doi.org/10.1021/jp709885n>.
- X. Han, Y. Li, H. Gong, Y. Wang, J. Lv, Y. Wang, S. Huang, X. Ma, Effect of Mn-dopant on carburization of the Fe_3O_4 catalysts in Fischer-Tropsch synthesis, *Chem. Eng. Sci.* X 11 (2021) 100106, <https://doi.org/10.1016/j.cesx.2021.100106>.
- X. Li, J. Paier, Vibrational properties of CO_2 adsorbed on the $\text{Fe}_3\text{O}_4(111)$ surface: insights gained from DFT, *J. Chem. Phys.* 152 (2020) 104702, <https://doi.org/10.1063/1.5136323>.
- D. Santos-Carballal, A. Roldan, R. Grau-Crespo, N.H. de Leeuw, A DFT study of the structures, stabilities and redox behaviour of the major surfaces of magnetite Fe_3O_4 , *Phys. Chem. Chem. Phys.* 16 (2014) 21082–21097, <https://doi.org/10.1039/C4CP00529E>.

[25] T.K. Shimizu, J. Jung, H.S. Kato, Y. Kim, M. Kawai, Termination and Verwey transition of the (111) surface of magnetite studied by scanning tunneling microscopy and first-principles calculations, *Phys. Rev. B* 81 (2010) 235429, <https://doi.org/10.1103/PhysRevB.81.235429>.

[26] A. Kiejna, T. Ossowski, T. Pabiszak, Surface properties of the clean and Au/Pd covered Fe_3O_4 (111): DFT and DFT+U study, *Phys. Rev. B* 85 (2012) 125414, <https://doi.org/10.1103/PhysRevB.85.125414>.

[27] X. Nie, L. Meng, H. Wang, Y. Chen, X. Guo, C. Song, DFT insight into the effect of potassium on the adsorption, activation and dissociation of CO_2 over Fe-based catalysts, *Phys. Chem. Chem. Phys.* 20 (2018) 14694–14707, <https://doi.org/10.1039/C8CP02218F>.

[28] G. Henkelman, B.P. Uberuaga, H. Jónsson, A climbing image nudged elastic band method for finding saddle points and minimum energy paths, *J. Chem. Phys.* 113 (2000) 9901, <https://doi.org/10.1063/1.1329672>.

[29] G. Henkelman, H. Jónsson, A dimer method for finding saddle points on high dimensional potential surfaces using only first derivatives, *J. Chem. Phys.* 111 (1999) 7010–7022, <https://doi.org/10.1063/1.480097>.

[30] H. Liu, C. Di Valentin, Band gap in magnetite above verwey temperature induced by symmetry breaking, *J. Phys. Chem. C* 121 (2017) 25736–25742, <https://doi.org/10.1021/acs.jpcc.7b09387>.

[31] F.N. Skomurski, S. Kerisit, K.M. Rosso, Structure, charge distribution, and electron hopping dynamics in magnetite (Fe_3O_4) (100) surfaces from first principles, *Geochim. Cosmochim. Acta* 74 (2010) 4234–4248, <https://doi.org/10.1016/j.gca.2010.04.063>.

[32] J.P. Wright, J.P. Attfield, P.G. Radaelli, Charge ordered structure of magnetite Fe_3O_4 below the Verwey transition, *Phys. Rev. B* 66 (2002) 214422, <https://doi.org/10.1103/PhysRevB.66.214422>.

[33] H. Okudera, K. Kihara, T. Matsumoto, Temperature dependence of structure parameters in natural magnetite: single crystal X-ray studies from 126 to 773 K, *Acta Crystallogr. B* 52 (1996) 450–457, <https://doi.org/10.1107/S0108768196000845>.

[34] P. Politzer, R.G. Parr, D.R. Murphy, Approximate determination of Wigner-Seitz radii from free-atom wave functions, *Phys. Rev. B* 31 (1985) 6809–6810, <https://doi.org/10.1103/PhysRevB.31.6809>.

[35] M. Fonin, Y.S. Dedkov, R. Pentcheva, U. Rüdiger, G. Güntherodt, Magnetite: a search for the half-metallic state, *J. Phys.: Condens. Matter* 19 (2007) 315217, <https://doi.org/10.1088/0953-8984/19/31/315217>.

[36] R. Aragón, Magnetization and exchange in nonstoichiometric magnetite, *Phys. Rev. B* 46 (1992) 5328–5333, <https://doi.org/10.1103/PhysRevB.46.5328>.

[37] Y. Meng, X.W. Liu, C.F. Huo, W.P. Guo, D.B. Cao, Q. Peng, A. Dearden, X. Gonze, Y. Yang, J. Wang, H. Jiao, Y. Li, X.D. Wen, When density functional approximations meet iron oxides, *J. Chem. Theory Comput.* 12 (2016) 5132–5144, <https://doi.org/10.1021/acs.jctc.6b00640>.

[38] W. Li, J.M. Arce-Ramos, M.B. Sullivan, C. Kok Poh, L. Chen, A. Borgna, J. Zhang, Mechanistic insights into selective ethylene formation on the χ - Fe_5C_2 (510) surface, *J. Catal.* 421 (2023) 185–193, <https://doi.org/10.1016/j.jcat.2023.03.014>.

[39] L.J.E. Hofer, E.M. Cohn, Saturation magnetizations of iron carbides, *J. Am. Chem. Soc.* 81 (1959) 1576–1582.

[40] J.J. Retief, Powder diffraction data and rietveld refinement of Hägg-carbide, χ - Fe_5C_2 , *Powder Diffr.* 14 (1999) 130–132, <https://doi.org/10.1017/S0885715600010435>.

[41] A.R. Lennie, N.G. Condon, F.M. Leibsle, P.W. Murray, G. Thornton, D.J. Vaughan, Structures of Fe_3O_4 (111) surfaces observed by scanning tunneling microscopy, *Phys. Rev. B* 53 (1996) 10244–10253, <https://doi.org/10.1103/PhysRevB.53.10244>.

[42] M. Creutzburg, K. Sellschopp, R. Gleißner, B. Arndt, G.B. Vonbun-Feldbauer, V. Vonk, H. Noei, A. Stierle, Surface structure of magnetite (111) under oxidizing and reducing conditions, *J. Phys. Condens. Matter* 34 (2022), <https://doi.org/10.1088/1361-648X/ac4d5a>.

[43] J. Noh, O.I. Osman, S.G. Aziz, P. Winget, J.-L. Brédas, Magnetite Fe_3O_4 (111) surfaces: impact of defects on structure, stability, and electronic properties, *Chem. Mater.* 27 (2015) 5856–5867, <https://doi.org/10.1021/acs.chemmater.5b02885>.

[44] T. Yang, J. Liu, Y. Wang, X. Wen, B. Shen, Structures and energetics of CO_2 adsorption on the Fe_3O_4 (111) surface, *J. Fuel Chem. Technol.* 46 (2018) 1113–1120, [https://doi.org/10.1016/S1872-5813\(18\)30044-6](https://doi.org/10.1016/S1872-5813(18)30044-6).

[45] T. Su, Z. Qin, G. Huang, H. Ji, Y. Jiang, J. Chen, Density functional theory study on the interaction of CO_2 with Fe_3O_4 (111) surface, *Appl. Surf. Sci.* 378 (2016) 270–276, <https://doi.org/10.1016/j.apsusc.2016.03.097>.

[46] M.R. Elahifard, M.P. Jigato, J.W. Niemantsverdriet, Direct versus hydrogen-assisted CO dissociation on the Fe (100) surface: A DFT study, *ChemPhysChem* 13 (2012) 89–91, <https://doi.org/10.1002/cphc.201100759>.

[47] W. Li, H. Wang, X. Jiang, J. Zhu, Z. Liu, X. Guo, C. Song, A short review of recent advances in CO_2 hydrogenation to hydrocarbons over heterogeneous catalysts, *RSC Adv.* 8 (2018) 7651–7669, <https://doi.org/10.1039/C7RA13546G>.

[48] E. de Smit, F. Cingnani, A.M. Beale, O.V. Safonova, W. van Beek, P. Sautet, B. M. Weckhuysen, Stability and reactivity of ϵ - χ - θ iron carbide catalyst phases in Fischer–Tropsch synthesis: controlling μ C, *J. Am. Chem. Soc.* 132 (2010) 14928–14941, <https://doi.org/10.1021/ja105853q>.

[49] A.S. W, Q. Yang, A.A. Matvienko, V.Y. Bychkov, Y.P. Tulenin, H. Lund, S.A. Petrov, R. Krahnert, A. Arinchtein, J. Weiss, A. Brueckner, E.V. Kondratenko, Understanding reaction-induced restructuring of well-defined $\text{Fe}_x\text{O}_y\text{C}_z$ compositions and its effect on CO_2 hydrogenation, *Appl. Catal. B* 291 (2021) 120121, <https://doi.org/10.1016/j.apcatb.2021.120121>.

[50] S. Saeidi, S. Najari, V. Hessel, K. Wilson, F.J. Keil, P. Concepción, S.L. Suib, A. E. Rodrigues, Recent advances in CO_2 hydrogenation to value-added products — Current challenges and future directions, *Prog. Energy Combust. Sci.* 85 (2021) 100905, <https://doi.org/10.1016/j.pecs.2021.100905>.

[51] Y. Liu, P.R. Murthy, X. Zhang, H. Wang, C. Shi, Phase transformation of iron oxide to carbide and Fe_3C as an active center for the RWGS reaction, *N. J. Chem.* 45 (2021) 22444–22449, <https://doi.org/10.1039/DINJ04120G>.

[52] X. Liu, C. Cao, P. Tian, M. Zhu, Y. Zhang, J. Xu, Y. Tian, Y.F. Han, Resolving CO_2 activation and hydrogenation pathways over iron carbides from DFT investigation, *J. CO₂ Util.* 38 (2020) 10–15, <https://doi.org/10.1016/j.jcou.2019.12.014>.

[53] M.D. Porosoff, S. Kattel, W. Li, P. Liu, J.G. Chen, Identifying trends and descriptors for selective CO_2 conversion to CO over transition metal carbides, *Chem. Comm.* 51 (2015) 6988–6991, <https://doi.org/10.1039/C5CC01545F>.

[54] J.R. Morse, M. Juneau, J.W. Baldwin, M.D. Porosoff, H.D. Willauer, Alkali promoted tungsten carbide as a selective catalyst for the reverse water gas shift reaction, *J. CO₂ Util.* 35 (2020) 38–46, <https://doi.org/10.1016/j.jcou.2019.08.024>.

[55] H.D. Willauer, R. Ananth, M.T. Olsen, D.M. Drab, D.R. Hardy, F.W. Williams, Modeling and kinetic analysis of CO_2 hydrogenation using a Mn and K-promoted Fe catalyst in a fixed-bed reactor, *J. CO₂ Util.* 3–4 (2013) 56–64, <https://doi.org/10.1016/j.jcou.2013.10.003>.

[56] S. De, A. Dokania, A. Ramirez, J. Gascon, Advances in the design of heterogeneous catalysts and thermocatalytic processes for CO_2 utilization, *ACS Catal.* 10 (2020) 14147–14185, <https://doi.org/10.1021/acscatal.0c04273>.

[57] D. Weber, T. He, M. Wong, C. Moon, A. Zhang, N. Foley, N.J. Ramer, C. Zhang, Recent advances in the mitigation of the catalyst deactivation of CO_2 hydrogenation to light olefins, *Catalysts* 11 (2021) 1447, <https://doi.org/10.3390/catal11121447>.

[58] W.D. Shafer, G. Jacobs, U.M. Graham, H.H. Hamdeh, B.H. Davis, Increased CO_2 hydrogenation to liquid products using promoted iron catalysts, *J. Catal.* 369 (2019) 239–248, <https://doi.org/10.1016/j.jcat.2018.11.001>.

[59] C. Zhang, C. Cao, Y. Zhang, X. Liu, J. Xu, M. Zhu, W. Tu, Y.-F. Han, Unraveling the role of zinc on bimetallic $\text{Fe}_5\text{C}_2\text{-ZnO}$ catalysts for highly selective carbon dioxide hydrogenation to high carbon α -olefins, *ACS Catal.* 11 (2021) 2121–2133, <https://doi.org/10.1021/acscatal.0c04627>.

[60] M. García-Melchor, N. López, Homolytic products from heterolytic paths in H_2 dissociation on metal oxides: the example of CeO_2 , *J. Phys. Chem. C* 118 (2014) 10921–10926, <https://doi.org/10.1021/jp502309r>.

[61] P. Sirikulbodee, M. Phongaksorn, T. Sornchamni, T. Ratana, S. Tungkamani, Effect of different iron phases of Fe/SiO_2 Catalyst in CO_2 hydrogenation under mild conditions, *Catalysts* 12 (2022) 698, <https://doi.org/10.3390/catal12070698>.

[62] M. Zhu, T.C.R. Rocha, T. Lunkenstein, A. Knop-Gericke, R. Schlägl, I.E. Wachs, Promotion mechanisms of iron oxide-based high temperature water-gas shift catalysts by chromium and copper, *ACS Catal.* 6 (2016) 4455–4464, <https://doi.org/10.1021/acscatal.6b00698>.

[63] W.K. Jozwiak, E. Kaczmarek, T.P. Maniecki, W. Ignaczak, W. Maniukiewicz, Reduction behavior of iron oxides in hydrogen and carbon monoxide atmospheres, *Appl. Catal. A Gen.* 326 (2007) 17–27, <https://doi.org/10.1016/j.apcata.2007.03.021>.

[64] T.C. Bromfield, D. Curulla Ferré, J.W. Niemantsverdriet, A DFT study of the adsorption and dissociation of CO on Fe(100): influence of surface coverage on the nature of accessible adsorption states, *ChemPhysChem* 6 (2005) 254–260, <https://doi.org/10.1002/cphc.200400452>.

[65] D.C. Sorescu, D.L. Thompson, M.M. Hurley, C.F. Chabalowski, First-principles calculations of the adsorption, diffusion, and dissociation of a CO molecule on the Fe(100) surface, *Phys. Rev. B* 66 (2002) 035416, <https://doi.org/10.1103/PhysRevB.66.035416>.

[66] K. He, Z. Zheng, Z. Chen, Multistep reduction kinetics of Fe_3O_4 to Fe with CO in a micro fluidized bed reaction analyzer, *Powder Technol.* 360 (2020) 1227–1236, <https://doi.org/10.1016/j.powtec.2019.10.094>.